# KRYPTON TAGGING VELOCIMETRY (KTV) IN SUPERSONIC TURBULENT BOUNDARY LAYERS

by

Drew Zahradka

A THESIS

Submitted to the Faculty of the Stevens Institute of Technology
in partial fulfillment of the requirements for the degree of

MASTER OF ENGINEERING - MECHANICAL

Drew Zahradka, Candidate

ADVISORY COMMITTEE

Nicholas J. Parziale, Advisor Date

Hamid Hadim, Reader Date

STEVENS INSTITUTE OF TECHNOLOGY
Castle Point on Hudson
Hoboken, NJ 07030
2015

# KRYPTON TAGGING VELOCIMETRY (KTV) IN SUPERSONIC TURBULENT BOUNDARY LAYERS

## ABSTRACT

The krypton tagging velocimetry (KTV) technique is applied to the turbulent boundary layer on the wall of the Mach 3 Calibration Tunnel at Arnold Engineering Development Complex (AEDC) White Oak. Profiles of velocity were measured with KTV and Pitot-pressure probes in the Mach 2.75 turbulent boundary layer comprised of 99% $N_2$/1% Kr at momentum-thickness Reynolds numbers of $Re_\Theta$ = 800, 1400, and 2400. Agreement between the KTV- and Pitot-derived velocity profiles is excellent. The KTV and Pitot velocity data follow the law of the wall in the logarithmic region with application of the Van Driest I transformation. Also, the velocity data in the wake region are consistent with data from the literature for a turbulent boundary layer with a favorable pressure gradient history. A modification of the Mach 3 AEDC Calibration Tunnel is described which facilitates operation at several discrete unit Reynolds numbers consistent with AEDC Hypervelocity Tunnel 9 run conditions of interest. Moreover, to enable near-wall measurement with KTV, an 800 nm longpass filter was used to block the reflection and scatter from the 760.2 nm read-laser pulse. With the longpass filter, the 819.0 nm emission from the re-excited Kr can be imaged to track the displacement of the metastable tracer without imaging the reflection and scatter from the read laser.

Author: Drew Zahradka

Advisor: Nicholas J. Parziale

Date: December 11, 2015

Department: Mechanical

Degree: Master of Engineering - Mechanical

**Acknowledgments**

I would like to thank Eric Marinaeu of AEDC White Oak for all of the theoretical guidance and support when it came to aspects of turbulent flow that were unknown to the author. Also, to Mike Smith of AEDC White Oak for all of the technical support in the lab. Mike Smith worked very closely with me in the lab and helped put many hours in to keep the experiment running smoothly. I would also like to thank my advisor Nick Parziale. Without his mentoring I would have never taken on this project. He has been most patient with me when subject matter was too advanced and took the time to teach me to better understand all aspects of this project.

The Air Force SFFP supported me and Professor Parziale with a stipend for this work. The facilities and equipment were supplied by the Arnold Engineering Development Center (AEDC). I would like to acknowledge the encouragement of John Laffery and Dan Marren of AEDC White Oak. I would like to thank Mr. Brooks for his technical help with the Pitot-tube measurements. I would also like to acknowledge Joseph Wehrmeyer at Aerospace Testing Alliance (AEDC) for providing some of the laser systems.

Lastly, I would like to thank my family for all their love and support. They are behind me in all my decisions, there to celebrate my successes and to help me learn from my failures.

Table of Contents

## List of Tables

## List of Figures

**List of Symbols**

| | |
|---|---|
| $\dot{m}$ | Mass-flow-rate, (kg/s) |
| $C$ | Discharge Coefficient, (-) |
| $A$ | Area, ($m^2$) |
| $\gamma$ | Ratio of specific heats, (-) |
| $\rho$ | Density, ($kg/m^3$) |
| $P$ | Pressure, (Pa) |
| $t$ | Time, (s) |
| $\tau$ | Timescale, (1/s) |
| $k_q$ | Quenching Rate Constant, ($cm^3$/(molecule s)) |
| $Ru$ | Universal Gas Constant ((Pa $m^3$)/(kg mol K)) |
| $T$ | Temperature, (K) |
| $M$ | Mach Number, (-) |
| $Re$ | Reynolds Number, (-) |
| $U$ | Velocity, (m/s) |
| $u_\tau$ | Friction velocity, (m/s) |
| $x$ | Distance, (m) |
| $r$ | Recovery Factor, (-) |
| $\Delta x$ | Displacement Distance, (m) |
| $\Delta t$ | Change in Time, (s) |
| $\Theta$ | Momentum Thickness, (m) |
| $\Delta^*$ | Integral Length Scale for Momentum Thickness, (m) |
| $c$ | Sound speed, (m/s) |

*Subscript*

| | |
|---|---|
| $OP$ | Orifice Plate |
| $A$ | Ambient |
| $noz$ | Nozzle |
| $R$ | Reservoir |
| $m$ | Metastable |
| $\infty$ | Free Stream |
| $\Theta$ | Based on Momentum Thickness |
| 02 | Pitot |
| $w$ | Wall |
| $e$ | Edge |
| $r$ | Recovery |

# Chapter 1

## Introduction

The need to accurately assess the heat transfer, skin friction, and velocity profiles on high-speed vehicles is born out of a thrust for rapid space access[1] and conventional prompt global strike (CPGS).[2] These properties are of importance because as vehicles reach high supersonic/hypersonic speeds, shock wave/boundary layer interactions can induce destructive high pressure and temperature loads and fluctuations on the surfaces of the vehicle.[3] At hypersonic speeds, aerodynamic heating is caused by the transformation of kinetic energy into internal energy. In the hypersonic regime, viscous interactions and the real-gas effects must be considered. Viscous interactions cause large values of pressure, skin friction and heat transfer coefficient. Real-gas effects further complicate the flow field, with features which may include chemistry and radiation.[3]

One way to assess these properties is by visualizing the velocity profile with velocimetry. Non-invasive velocimetry techniques are used in turbulent and complex flow fields due to the lack of disruptions to the flow field. Some techniques include various methods of Doppler velocimetry, particle image velocimetry (PIV) and tagging velocimetry. Doppler velocimetry and PIV pose issues of particle selection and sizing and may present serious velocity lag issues and harm to the testing material. Issues with tagging velocimetry in complex flows arise due to the reactivity of the particles that are imaged. A new method, which is proposed in this thesis, is Krypton tagging velocimetry (KTV). KTV is a type of tagging velocimetry which utilizes Krypton atoms as the particle and relies on the excitation of atoms to image the flow field.

Due to the inert properties of Krypton, there are no worries issues of reactivity.

In this thesis, I first present the KTV setup and excitation/emission scheme with the longpass filter in place. I present KTV results with the new excitation/emission scheme as applied to an underexpanded jet to assess the SNR. I then describe a modification of the Mach 3 AEDC Calibration Tunnel which facilitates operation at several discrete unit Reynolds numbers consistent with AEDC Hypervelocity Tunnel 9 run conditions of interest. I present KTV and Pitot-probe based velocity measurements for a Mach 2.75 turbulent boundary layer. Finally, I non-dimensionalize the velocimetry results, first with application of the Van Driest I transformation, and lastly with a scaling of the data in the wake region.

# Chapter 2

# Literary Review

Visualizing the velocity profile reveals many characteristics about the flow field, such as: boundary layer thickness, assessment of laminar/turbulent flow, if there is velocity slip at the wall, and whether there is flow separation. These characteristics can be used to determine the heat transfer and skin friction on the surface of the vehicle in question. The heat transfer rate and skin friction are driving parameters when it comes to material selection, vehicle profile and the design of a thermal protective system (TPS).

## 2.1 Design Considerations

Two types of vehicles that experience hypersonic flight include 1) the vehicle is either placed in orbit by a rocket propulsion system and then returns to earth as an unpowered glider, or 2) powered by an airbreathing propulsion system and must fly at altitudes low enough so there is sufficient oxygen for the system to operate. Vehicles re-entering the atmosphere experience extreme speeds and an extreme amount of heat transfer to the TPS. One major difficulty for designers of re-entry vehicles is predicting the flowfield at these conditions, especially modeling turbulent boundary layers. Vehicles powered by airbreathing propulsion systems typically have high convective heat transfer and drag due to an increase in density at lower altitudes.

One challenge for designing high-speed vehicles is the design of the propulsion system.[4] The vehicle experiences modes of subsonic, supersonic and hypersonic flight. To account for this, an engine is designed with a conventional ramjet cycle and a low-

speed engine cycle, forming a combined cycle engine.[5] The next issue is choosing the type of fuel. If hydrogen is used as the fuel source, a larger fuel tank is required, leading to an increase in skin-friction drag and surface heating. If a hydrocarbon is used, it has a lower heat capacity and may not provide sufficient cooling for Mach numbers over 7 or 8.[4] Also, the trajectory of the vehicle plays a key factor in design. The vehicle has to be designed so that as it climbs to cruising altitude and speed, "the external heat transfer loads are of such a magnitude that they could be absorbed by the fuel heat sink, while still having a configuration of sufficiently low drag."[6] The designers use many tools to create conceptual designs that allow for modeling the fluid flow in order to create the optimal design, including computational methods and ground testing, often in concert.

Progress has been made in the computation of high-speed and reacting flows, as reviewed in Candler[7] and Schwartzentruber and Boyd.[8] Different numerical methods include conventional computational fluid dynamics (CFD) and direct simulation Monte Carlo method (DSMC). DSMC uses particle simulation methods to produce simulations of hypersonic flow. DSMC enables proper modeling at large Knudsen numbers, where there is rarefaction and strong thermochemical effects. CFD simulation uses the Navier-Stokes equations and is used to model flows at low Knudsen numbers. Using the DSMC and CFD methods in conjunction enable designers to model gas flows spanning the appropriate Knudsen range typical of a hypersonic vehicle.[8]

Ground testing can be used to validate and calibrate numerical methods. Different types of ground-testing facilities to replicate different conditions of hypersonic flows include shock tunnels, arc-heated test faciliteis, heated Lidwig tubes, blow down hypersonic wind tunnels and ballistic free-flight ranges. Ground-testing proves very

valuable to replicate certain parameters of flight. No one type of ground-testing facility could replicate every aspect of flight, so certain facilities are used to replicate specific parameters. For example, in blow down hypersonic wind tunnels, to replicate high Mach number, the local sound of speed is often reduced by reducing the local temperature in a nozzle expansion, which precludes the study of thermochemistry.[4] To simulate the thermochemical effects associated with hypersonic flow, shock tunnels are used.

There is uncertainty that arises from the application of the state-of-the-art (SOA) research codes to hypersonic problems, which has been characterized in Bose et al.[9] These uncertainties come from fluid-dynamic phenomena that remain difficult to model. There is a lack of validation data for high-speed flowfields, and this complicates the development of SOA codes.

The computation of the heat transfer and skin friction requires detailed resolution of the flow very near to the wall. SOA diagnostics are still being developed to obtain resolution of turbulent flow velocity profiles near the wall. Obtaining test and evaluation (T&E) data for high-speed vehicle development[10]and validation data for SOA research codes is the motivation for the development of new experimental diagnostics, especially in demanding testing environments. Velocimetry results can be used to verify computational codes, enabling higher confidence in vehicle performance predicitions.

## 2.2 Velocimetry Techniques

There are a number of methodologies for making velocity measurements in fluid flows such as pressure-based measurement, thermal anemometry, and particle based tech-

niques (laser-Doppler velocimetry, global-Doppler velocimetry, and particle image velocimetry (PIV)).[11] The measurement of velocity with pressure-based and thermal anemometry methods are refined in that they can consistently yield data with low uncertainty; however, these techniques are intrusive, which eliminates them as candidates in certain flow regimes. Moreover, frequency response, spatial resolution, and required assumptions regarding the local temperature are limitations for velocity measurement using Pitot probes.

Particle-based methods of velocimetry can currently produce multi-component data and can yield field information about vorticity and pressure with post processing. Each of the particle-based methods utilize different methods to capture light scattered off or emitted by particles in the flow to make velocity measurements. Doppler velocimetry utilizes Doppler shift detection to measure flow velocity distributions. Laser-Doppler velocimetry (LDV) uses a dual-beam laser setup. Two focused laser beams are crossed over the flow field and illuminate seeded particles from different directions. The light scattered from illuminated particles experience a frequency shift dependent on the direction of the illumination and the velocity of the particles due to the Doppler effect. Superposition of the different frequency shifted signals creates interference on a detector, which can be either a high-speed camera or a smart pixel imaging array. The interference leads to a signal, which is modulated by the difference of the two Doppler shifts and the modulated frequency is dependent on the crossing angle of the two beams and velocity of the particles.[12] Global-Doppler velocimetry (DGV) utilizes the same principles of velocity detection as LDV, where the velocity is determined based on the frequency shift. However, it differs from LDV by allowing for the measurement of the planar velocity distribution. DGV illuminates the flow field with a laser sheet, rather than two focused beams. This allows for the measurement

of planar three-component velocity data. DGV has been successfully implemented in full scale wind tunnels, high-speed flows and combustion measurements.[13]

Some issues that arise with Doppler velocimetry is particle selection. The velocity measured is the velocity of the particle, not of the actual flow. This can lead to potential velocity lag, pending on the size and distribution of the particles in the flow. If velocity lags are not recognized, discrepancies between experimental and computational solutions may be greater leading to an increase in error.[14] Solid particles can be used for Doppler velocimetry as well. Some solid particles are introduced in the flow in a carrier solution. This presents issues because the solution can evaporate before reaching the the test section and seed size is small, making it more difficult to get an accurate measurement. Other solid seeds are introduced with a fluidized-bed-type seeder.[14] These particles can be abrasive to the model, leading to damage and inaccurate measurements.

Particle Imaging Velocimetry (PIV) is a technique where seeded particles scatter laser light and the displacement of the particle is measured to find the velocity of the flow. The seeded particle in gas flows must be chosen carefully. This is because the density difference between the gas and the particle can lead to a significant velocity lag. Particles are injected in the gas either locally or globally. As the fluid enters the test section a laser pulse illuminates the particles. A second pulse is sent after a time delay to illuminate the particles a second time and the displacement of the particles is used to find their velocity. The particle displacement is captured using a camera and the velocity is found by processing the data. Ideally, the velocity of the particles is very similar to the velocity of the flow. However, to have the agreement between the particle velocity and the flow velocity, the size of the particles must be small. This presents an issue with illumination because larger particles scatter light

more effectively. An optimal particle size must be determined when performing PIV so that the particle can scatter enough light to be imaged but is also small enough so that the velocity of the particle does not significantly lag the velocity of the fluid. Currently, the PIV technique is difficult to implement in large-scale wind tunnels. A major issue for implementation is that the wind tunnels are very large, which means there is a significant distance between the observation site, the light source and the imaging source. In order for the scattered light to reach the imaging source, larger particles or an extremely powerful pulse laser needs to be used to illuminate the flow field. Timing issues also present themselves when implementing PIV in impulse facilities such as shock tunnels.[15]

An additional velocimetry technique is tagging velocimetry (TV) which will be the main focus of this thesis. It is a optical technique that relies on turning molecules into long lifetime tracers by exciting them at proper wavelengths.[16] The excited molecules are typically native to the gas, seeded into the gas, or synthesized by a reaction within the gas. The luminescence from the molecules that TV relies on is either fluorescence or phosphorescence, depending on which technique is used. The tracer lifetime of a fluorescent molecule is shorter than that of a phosphorescent molecule because the transition of a fluorescent molecule from excited to ground state is allowed, whereas that transition is forbidden for a phosphorescent molecule.[16] The molecules are excited with the use of a laser that emits photons at specific wavelengths. The simplest method of molecular tagging creates tagged lines perpendicular to the flow direction and captures the displacement of the lines to calculate the velocity. A high speed camera, is placed perpendicular to the tagged line and takes delayed images to find the displacement of the lines. One issue with line tagging is that it only allows for the measurement of one component of velocity; however, researchers

are making progress by tracking grids.

One benefit of TV, relative to particle based methods, is that when tagging molecules, the velocity of the tagged constituent faithfully follows the velocity of the flow. When tagging a constituent, the lag is negligible, and the velocity measured is the velocity of the field. Noted methods of tagging velocimetry include the VENOM,[17–21] APART,[22–24] RELIEF,[25–29] iodine,[30,31] acetone,[32–34] and the hydroxyl group[35–37] techniques among others.[38–41] Molecular tagging can offer many advantages where particle-based techniques that rely on seeded particles prove undesirable, difficult or may lead to complications. In contrast to the limitations of implementing PIV techniques in high-speed facilities, the implementation of tagging velocimetry is not limited by timing issues associated with tracer injection or reduced particle response at Knudsen and Reynolds number typical of high-speed windtunnels.

## 2.3 AEDC Tunnel 9

One blowdown facility, which is the end goal facility for implementation of the technique discussed in this thesis, is AEDC Hypervelocity Tunnel 9. The following description of AEDC Hypervelocity Tunnel 9 is described in the article by Lafferty and Marren.[42] Tunnel 9 is a blow down hypersonic wind tunnel that uses pure nitrogen as the working fluid. It can operate at several Mach numbers, 7, 8, 10, 14, and 16.5, depending on the nozzle that is used.[42] The test section allows for full-scale analysis of reentry and intercepter configurations. It is over 12 feet long and is 5 feet in diameter.[42] During a typical run, the nitrogen is heated and pressurized in a vessel to predetermined conditions. The test section is evacuated and when the nitrogen reaches the predetermined conditions, the diaphragm that separates the test section

from the vessel ruptures.

# Chapter 3

# Experimental Setup

## 3.1 Krypton Tagging Velocimetry (KTV) Experimental Setup

Krypton Tagging Velocimetry (KTV),[43,44] relative to other tagging velocimetry techniques, relies on a chemically inert tracer. This property may enable KTV to broaden the utility of tagging velocimetry because the technique can be applied in gas flows where the chemical composition is difficult to prescribe or predict. The use of a metastable noble gas as a tagging velocimetry tracer was first suggested by Mills et al.[45] and Balla and Everhart.[46] KTV was first demonstrated by Parziale et al.[43,44] to measure the velocity along the center-line of an underexpanded jet of $N_2$/Kr mixtures. In that work, pulsed tunable lasers were used to excite and/or induce fluorescence of Kr atoms that were seeded into the flow for the purposes of position tracking.

The excitation/emission scheme used in this work is slightly different than in the original work by Parziale et al.[43,44] A high-precision 800 nm longpass filter (Thorlabs FELH0800) is used to block the read-laser beam with the intent of minimizing the noise resulting from the read-laser pulse reflection and scatter from solid surfaces. This was done to enable the imaging of fluorescing Kr atoms near the windtunnel wall.

Following the energy level diagram in Fig. 3.1, KTV is performed as follows:
**1)** Seed a base flow with krypton locally or globally.
**2)** Photosynthesize metastable krypton atoms with a pulsed tunable laser to form the tagged tracer: two-photon excitation of $4p^6(^1S_0) \rightarrow 5p[3/2]_2$ (214.7 nm) and rapid

decay to metastable states $5p[3/2]_2 \rightarrow 5s[3/2]^o_1$ (819.0 nm) and $5p[3/2]_2 \rightarrow 5s[3/2]^o_2$ (760.2 nm).

**3)** Record the translation of the tagged metastable krypton by imaging the laser induced fluorescence (LIF) that is produced with an additional pulsed tunable laser: re-excite $5p[3/2]_2$ level by $5s[3/2]^o_2 \rightarrow 5p[3/2]_2$ transition with laser sheet (760.2 nm) and read spontaneous emission of $5p[3/2]_2 \rightarrow 5s[3/2]^o_1$ (819.0 nm) transitions with a camera positioned normal to the flow.

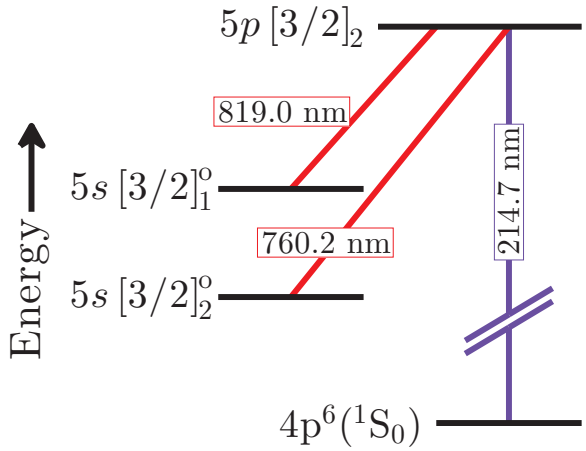


Figure 3.1: Energy level diagram for KTV.

The experiment was run using two sets of tunable lasers to provide the 214.7 nm (write) and 760.2 nm (read) laser beams required for KTV (schematic in Fig. 3.2). The write laser consisted of a frequency tripled PR8010 Nd:YAG laser and a frequency doubled Continuum ND6000 Dye Laser. The Nd:YAG laser pumped the dye laser with 400mJ/pulse at a wavelength of 355 nm. The dye in the laser was Coumarin 440 and the laser was tuned to output a 429.4 nm beam. Frequency doubling of the dye laser output was preformed using an Inrad BBO-C (65°) crystal placed in a Inrad 820-360 gimbal mount, resulting in a laser beam with two wavelengths, 214.7 nm and 429.4 nm. The 214.7 nm and 429.4 nm beams were separated with a Pellin-Broca prism. The 429.4 nm wavelength beam was sent to a beam dump and the 214.7 nm

wavelength beam was directed to the test section. The read laser consisted of a frequency doubled Continuum NY82S-10 Nd:YAG laser and a Continuum ND60 Dye Laser. The Nd:YAG laser pumped the dye laser with 250mJ/pulse at a wavelength of 532 nm. The dye in the laser was LDS 765 and the laser was tuned to output a 760.15 nm beam.

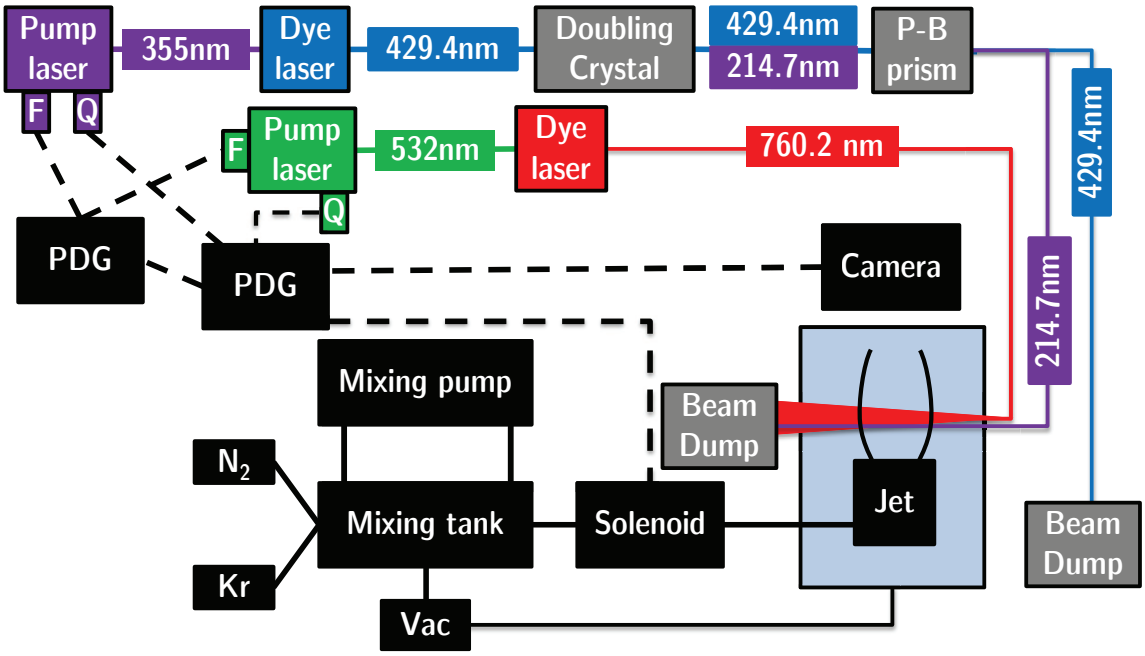


Figure 3.2: Setup of bench test experiment with lasers, test section, and appropriate wavelengths of laser beams.

The write-laser beam setup resulted in approximately 1 mJ/pulse, with a wavelength of 214.7 nm, a linewidth of approximately 10 $cm^{-1}$, a pulsewidth of approximately 7 ns, and a repetition rate of 10 Hz. The write-laser beam was directed into the test section with 1 inch 5th-harmonic Nd:YAG laser mirrors (IDEX Y5-1025-45) and focused to a narrow waist into the test section with a 1000 mm fused silica lens. Assuming Gaussian beam propagation, the waist diameter was $\approx$ 55 µm, the peak beam fluence was $\approx$ 21 J/$cm^2$, and the Rayleigh length was $\approx$ 44 mm. This narrow laser beam photosynthesizes the metastable krypton atoms that comprise the tracer

forming the “write line."

The read-laser beam setup resulted in approximately 20 mJ/pulse, with a wavelength of 760.15 nm, a linewidth of approximately 10 $cm^{-1}$, a pulsewidth of approximately 8 ns, and a repetition rate of 10 Hz. The read-laser beam was directed into the test section using 2 inch broadband dielectric mirrors (Thorlabs BB2-E02) as a sheet of $\approx$ 200 µm thickness. This “read sheet" re-excites the metastable Kr tracer atoms so that their displacement can be measured.

The read sheet must overlap the write line at the anticipated position after the delay between the write and read laser pulses. Example burn patterns that illustrate the beam locations prior to performing an experiment are presented as Fig. 3.3(a). In Fig. 3.3(b), the “hot" portion of the laser beams are identified with a narrow, red ellipse indicating the approximate spatial bound of the read sheet and a violet circle indicating the same of the write line. Note that these are not indicative of beam size because the burn patterns are produced after approximately 10 pulses from the write and read lasers, which tend to overexpose the burn paper.

The laser and camera timing is controlled by pulse/delay generators. The flash lamps and the Q-switches of the Nd:YAG lasers are triggered to cycle at 10 Hz by one pulse/delay generator (SRS DG535). Another pulse/delay generator (SRS DG535) is used to control camera timing and gate width. For the underexpanded jet experiments, an additional BNC 505-4C pulse/delay generator is set to single-shot mode to trigger the solenoid to the jet.

The intensified camera used for all experiments is a 16-bit Princeton Instruments PIMAX-2 1024x1024 with an 18 mm Gen III Extended Blue intensifier. The gain is set to 255 with 2x2 pixel binning to ensure a 10 Hz frame rate. The cam-

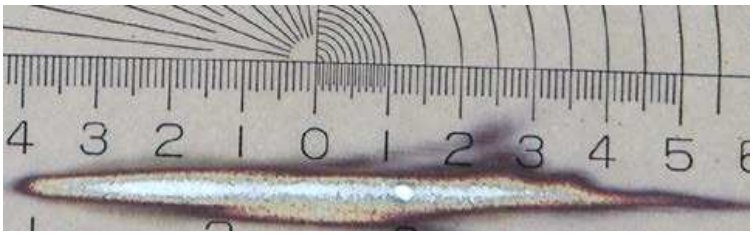

(a)

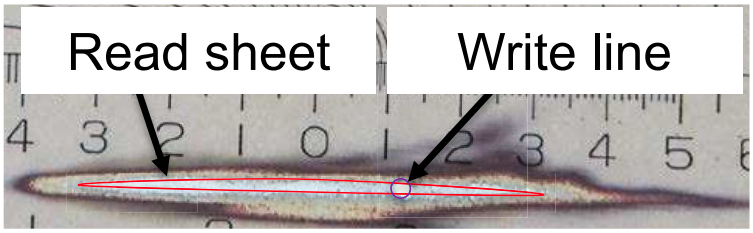


(b)

Figure 3.3: Burn pattern overlaps of the write and read lasers. Size is illustrated in (a) and the “hot" portion of the beams are annotated in (b). The ruler in the background is in millimeters.

era gate was opened for 50 ns to bracket the read-laser pulse so as to capture the spontaneous emission of $5p[3/2]_2 \rightarrow 5s[3/2]_1^o$ (819.0 nm) transitions.

### 3.2 Mach 2.75 AEDC Calibration Tunnel and Modification

The purpose of conducting KTV experiments in the Mach 3 AEDC Calibration Tunnel was to demonstrate that the technique could be utilized in AEDC Hypervelocity Tunnel 9,[42,47] which is a large-scale $N_2$ blow-down hypersonic windtunnel. The Mach 3 AEDC Calibration Tunnel is a large vacuum tank with a converging-diverging nozzle attached to it. To start the tunnel, a valve is cycled downstream of the nozzle throat. With the original setup, the effective reservoir is the ambient laboratory air and so the freestream conditions are fixed.

The Mach 3 AEDC Calibration Tunnel and AEDC Tunnel 9 operate with different run conditions; that is, AEDC Tunnel 9 typically operates with a lower

freestream pressure than does the Mach 3 AEDC Calibration Tunnel. This has implications on the SNR of the KTV technique because of the population available for fluorescence[48] and the quenching of the metastable Kr tracer.

To account for the difference in pressure, modifications were made to the tunnel upstream of the nozzle (boxed in red in Fig. 3.4). The effective reservoir pressure was reduced by choking the flow upstream of the throat with an orifice plate. A PVC pipe housed perforated screens that were used to breakup the jet from the orifice plate which was a PVC end cap with a hole drilled in it. Three caps with holes of diameter 12.7 mm, 19.1 mm, and 25.4 mm were used to alter the mass-flow rate, and thus the effective pressure drop.

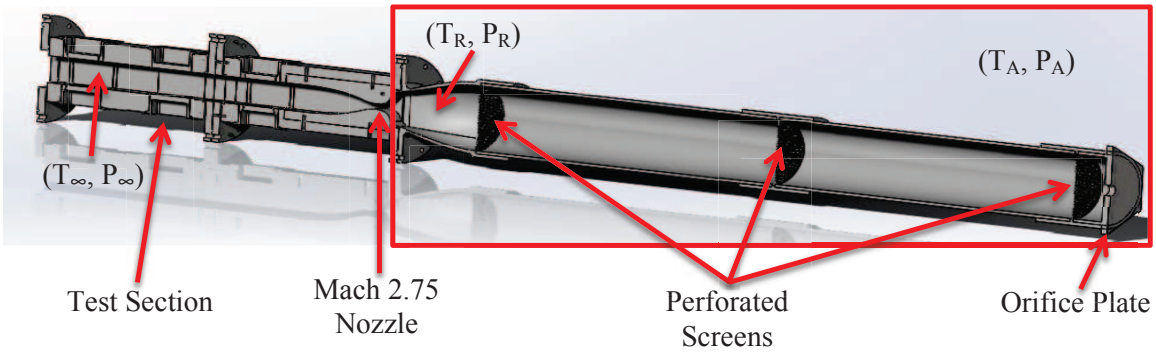


Figure 3.4: Test section of Mach 3 AEDC Calibration Tunnel and modification. The modification is boxed in red.

To estimate the reduced reservoir pressure, choked flow calculations[49] were used where sonic flow was assumed at the orifice plate and nozzle throat. The mass-flow-rate of the gas into the tube from the ambient lab to the effective reservoir was determined using

$$\dot{m} = C_{\mathrm{OP}} A_{\mathrm{OP}} \sqrt{\gamma \rho_A P_A \left(\frac{2}{\gamma+1}\right)^{\frac{\gamma+1}{\gamma-1}}} \tag{3.1}$$

and then the mass-flow-rate of the gas into the tube from effective reservoir to the

freestream was determined using

$$\dot{m} = C_{\text{noz}} A_{\text{noz}} \sqrt{\gamma \rho_R P_R \left(\frac{2}{\gamma+1}\right)^{\frac{\gamma+1}{\gamma-1}}} \tag{3.2}$$

where the subscripts “OP" and “noz" refer to the orifice plate and the nozzle, respectively. We assume that the flow is steady so that the mass-flow-rates in Eqs. 3.1 and 3.2 must match. Furthermore, we assume that the discharge coefficients, $C_{\text{OP}}$ and $C_{\text{noz}}$ are unity and that there are no standing shock waves wihtin the tube (no change in total pressure). Equating Eqs. 3.1, and 3.2 and solving for $P_R$ results in

$$P_R = P_A \sqrt{\frac{T_R}{T_A}} \frac{A_{\text{OP}}}{A_{\text{noz}}}. \tag{3.3}$$

Assuming that the expansion through the orifice plate and perforated screens (refer to Fig. 3.4) is isothermal, we find that the effective reservoir pressure could be reduced by a factor of approximately 2, 4, and 10 for the 25.4 mm, 19.1 mm, and 12.7 mm orifice plates, respectively. Predicted freestream static pressure values for the 25.4 mm, 19.1 mm, and 12.7 mm orifice plates are 1920 Pa, 1080 Pa, and 480 Pa, respectively; these predicted static pressures are within 10% of the measured static pressures in Table 3.1. Ultimately, we are interested in the effect of orifice plate diameter on the freestream unit Reynolds number, and the predicted unit Reynolds number is presented as Fig. 3.5. These calculations yield a promising strategy for controlling the Reynolds number of the flow in the Mach 3 AEDC Calibration Tunnel.

An isolation bag was added to the end of the tube over the orifice plate which isolates the test gas from the ambient air in the laboratory. The bag is flexible, so the test gas in the isolation bag is at constant ambient pressure throughout an experiment.

The test section, PVC tube, and isolation bag are filled with high-purity mixtures of nitrogen and krypton prior to an experiment. The Mach 3 AEDC Calibration Tunnel experiment, with the modification, is shown in Fig. 3.6.

The run conditions with each of the orifice plates were calculated by measuring the static and Pitot pressure with Micro Switch 130PC pressure transducers, and finding the freestream Mach number with the Rayleigh-Pitot probe formula[50]

$$\frac{P_{02}}{P_\infty} = \left( \frac{(\gamma+1)^2 M_\infty^2}{4\gamma M_\infty^2 - 2(\gamma-1)} \right)^{\left(\frac{\gamma}{\gamma-1}\right)} \left( \frac{1-\gamma+2\gamma M_\infty^2}{\gamma+1} \right). \tag{3.4}$$

The freestream temperature (and thus freestream velocity) were found by assuming

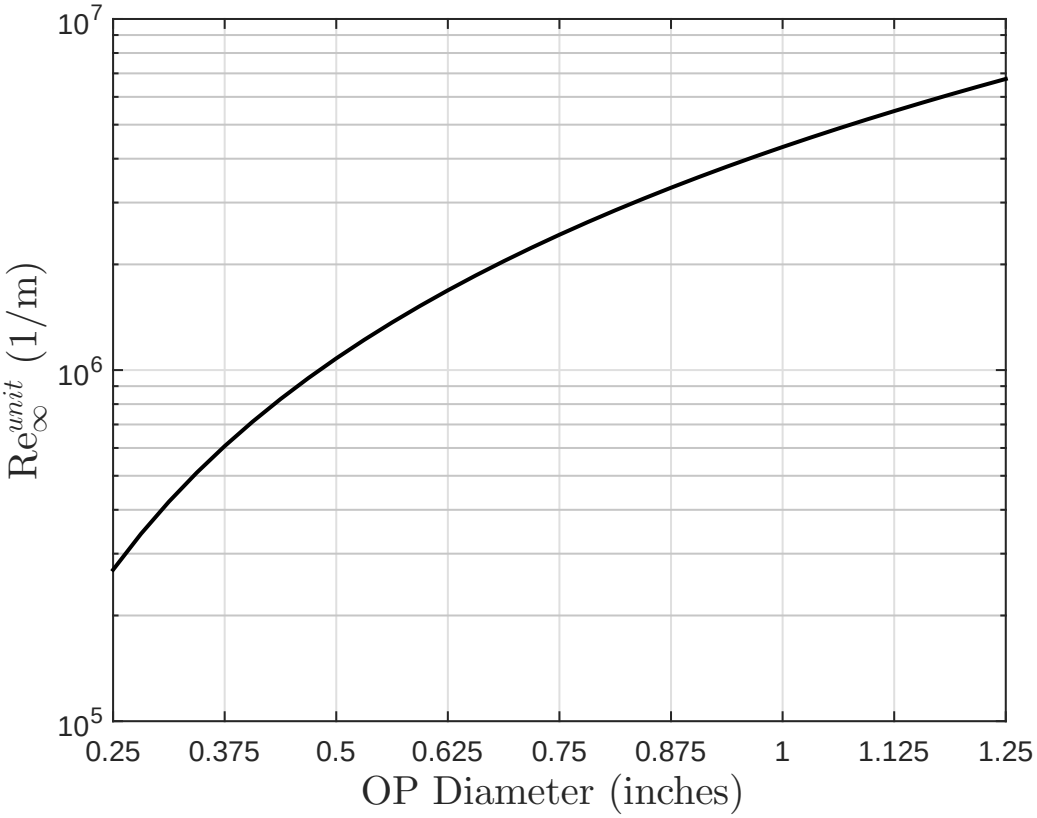


Figure 3.5: Predicted freestream unit Reynolds vs. orifice plate diameter.

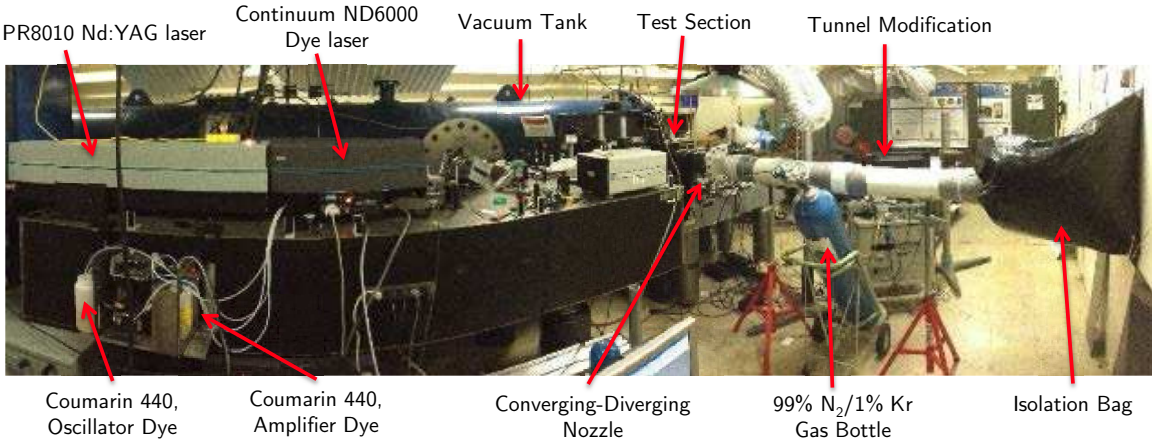


Figure 3.6: Mach 3 AEDC Calibration Tunnel experiment setup with annotations. Components not shown: NY82S-10Nd:YAG laser, Continuum ND60 Dye Laser and LDS 765 Amplifier and Oscillator Dye. The two lasers are located behind the write laser setup and the dye is located on the other side of the optical table.

isentropic expansion[50] as

$$T_\infty = T_R \left(1 + \frac{\gamma - 1}{2} M_\infty^2\right)^{-1}. \tag{3.5}$$

It was determined that the expansion through the orifice plates and perforated screens was isothermal by thermocouple measurement of the reservoir temperature using an Omega 5TC-TT-E-40-36 thermocouple; that is $T_R = T_A$ in Fig 3.4. Freestream conditions for each orifice plate are listed in Table 3.1. Example measurements for the static pressure, Pitot pressure, and reservoir temperature are presented in Fig. 3.7(a); the freestream Mach number is presented as Fig. 3.7(b). The expansion wave that propagates through the PVC tube during tunnel startup can be seen between 0.75-2.0 seconds. The steady test time is approximately 3 seconds (between 2 and 5 seconds).

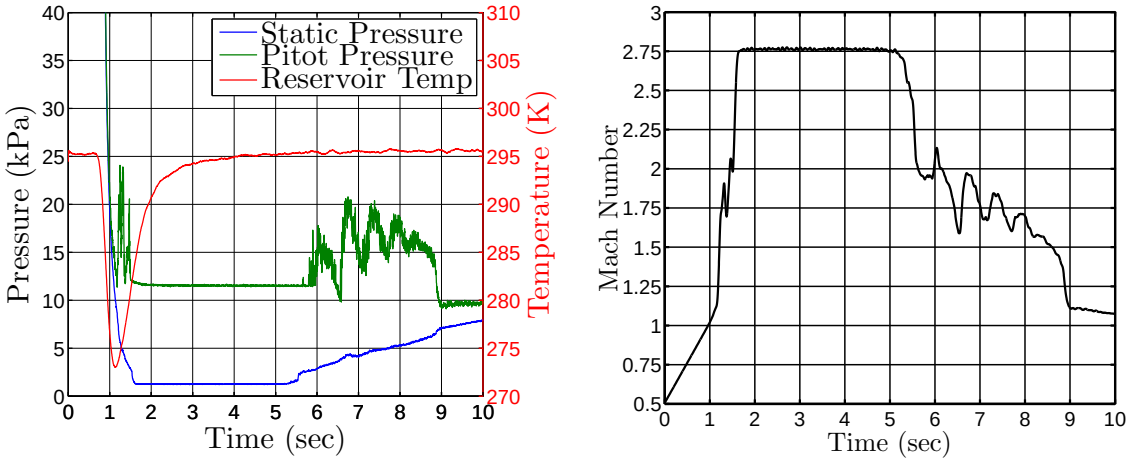


(a) (b)

Figure 3.7: Sample run conditions for the Mach 3 AEDC Calibration Tunnel for the 19.1 mm orifice plate. In (a), measurements of the static pressure, Pitot pressure, and reservoir temperature, used for the calculation of Mach number (b), and freestream velocity. The steady test time is observed to occur between approximately 2 and 5 seconds.

| Experiment | $M_\infty$ (-) | $P_\infty$ (Pa) | $T_\infty$ (K) | $\rho_\infty$ (kg/m$^3$) | $\mathrm{Re}_\infty^{unit}$ (1/m) | $\mathrm{Re}_\Theta$ (-) | $U_\infty$ (mm/µs) | $\tau_m$ (µs) | $x_m$ (mm) |
|---|---|---|---|---|---|---|---|---|---|
| Underexpanded Jet | 5.00 | 340 | 49.3 | 0.024 | 79.7e6 | - | 0.714 | 4.5 | 3.2 |
| Mach 3 AEDC Calibration Tunnel - 12.7 mm OP | 2.75 | 550 | 118 | 0.016 | 1.26e6 | 800 | 0.614 | 7.6 | 4.7 |
| Mach 3 AEDC Calibration Tunnel - 19.1 mm OP | 2.77 | 1010 | 118 | 0.030 | 2.30e6 | 1400 | 0.612 | 4.1 | 2.5 |
| Mach 3 AEDC Calibration Tunnel - 25.4 mm OP | 2.73 | 1825 | 118 | 0.053 | 4.16e6 | 2400 | 0.611 | 2.1 | 1.4 |
| AEDC Tunnel 9 Run 3742 | 9.86 | 600 | 53.4 | 0.038 | 15.0e6 | - | 1.469 | 3.15 | 4.6 |
| Caltech T5 Shot 2773 | 5.93 | 6000 | 1014 | 0.020 | 1.80e6 | - | 3.860 | 5.98 | 23 |

Table 3.1: Conditions for the estimation of the distance between the write and read locations for KTV in various experiments. $M_\infty$, $P_\infty$, $T_\infty$, $\rho_\infty$, $\mathrm{Re}_\infty^{unit}$, $\mathrm{Re}_\Theta$, and $U_\infty$ are the Mach number, pressure, temperature, density, unit Reynolds number, momentum thickness Reynolds number, and velocity scale for each experiment. $\tau_m$ and $x_m$ are the calculated time and distance scale for the decay of the metastable Kr state.

# Chapter 4

# Results/Discussion

## 4.1 Underexpanded Jet

In this chapter, I present the setup and results of an underexpanded jet comprised of a 99% $N_2$/1% Kr mixture. The purpose of this series of experiments was to recreate the results in Parziale et al.[43,44] while assessing the SNR with the modified excitation/emission scheme that utilizes a 800 nm longpass filter. In Parziale et al.,[43,44] the 760.2 nm and 819.0 nm transitions were imaged after re-excitation, refer to Fig. 3.1. With the 800 nm longpass filter in place, some signal would be lost; however, the noise resulting from the scatter and reflection of the read laser at 760.2 nm would be reduced as well.

The metastable krypton tracer is written approximately two diameters from an underexpanded jet orifice. A series of 6 exposures is presented as Fig. 4.1. In this series, the camera gate is chosen to bracket only the spontaneous emission of $5p[3/2]_2 \rightarrow 5s[3/2]_1^o$ (819.0 nm) transitions. The modified scheme reproduces the results from Parziale et al.,[43,44] but with a high-precision 800 nm longpass filter in place to block the noise resulting from the reflection and scatter of the 760.2 nm read sheet from solid surfaces. Ultimately, the signal-to-noise ratio (SNR) in Fig. 4.1 was sufficient to justify using this excitation/emission strategy in the Mach 3 AEDC Calibration Tunnel.

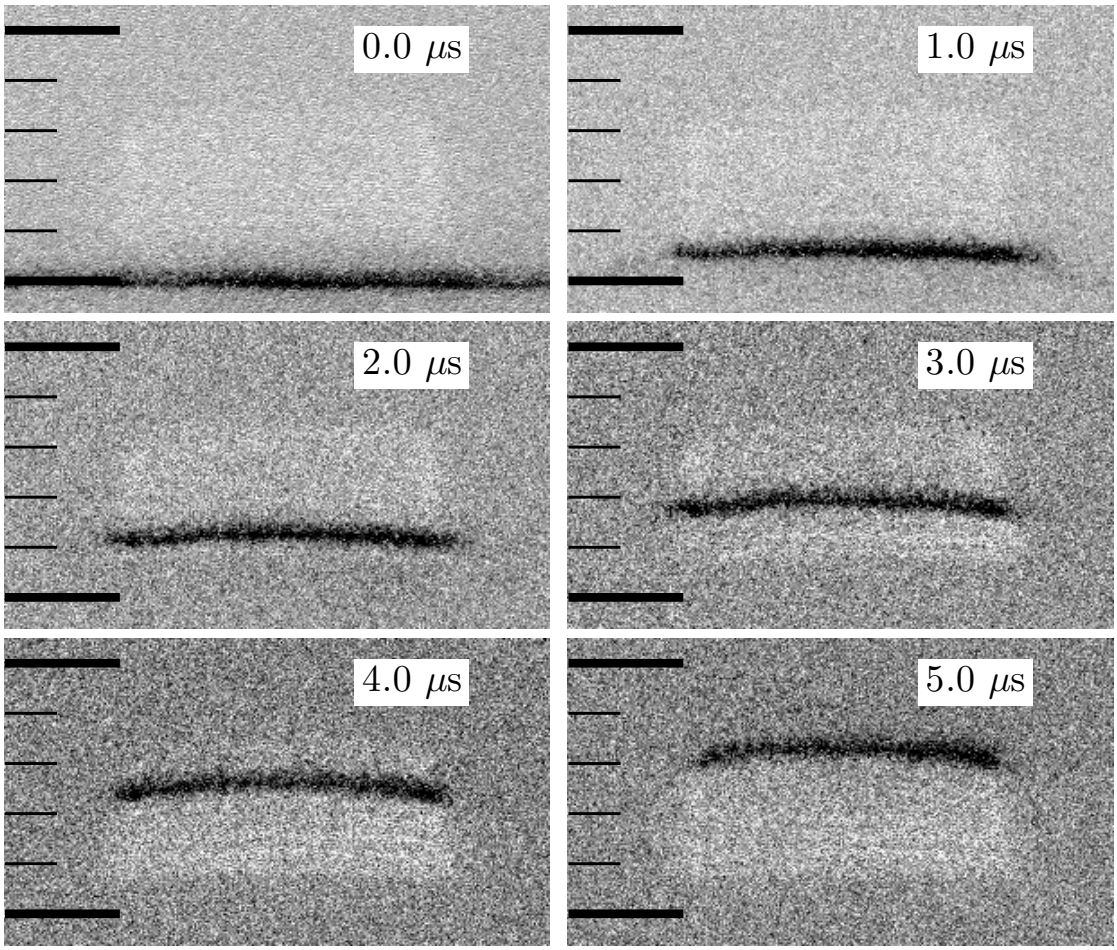


Figure 4.1: KTV in a 99% $N_2$/1% Kr underexpanded jet. Inverted intensity scale. The camera gate is fixed to include only the read laser pulses (after the first image). The time stamp of the delay between the write and read pulses is given in µs. Major tick marks at 5 mm intervals.

## 4.2 Effect of Run Condition on Metastable Lifetime

The SNR of a fluorescence technique is proportional to the local number density of the fluorescing constituent.[48] However, in the case of KTV, increasing the local number density also increases the decay rate of the photosynthesized metastable Kr $5s[3/2]_2^o$ tracer. This presents the researcher with the task of balancing the SNR with the lifetime of the tracer. In this section, we present estimates of the relevant figures

pertaining to the de-excitation rate of the metastable Kr tracer for flows of interest.

Researchers have studied the quenching rates of the $5s[3/2]_2^o$ state with a number of collisional partners.[51–54] In the work of Velazco et al.,[52] they tabulate the quenching rate constants of the $5s[3/2]_2^o$ with constituents of interest in the aerothermodynamics and combustion communities. Using the plug flow approximation, they used a flow reactor to determine the timescale of metastable state decay as

$$\frac{1}{\tau_m} = \frac{D_0}{\Lambda^2 P} + k_1 P + k_2 P + k_Q[Q], \tag{4.1}$$

where the first three terms are due to diffusion, and two-body and three-body de-excitation processes in the argon carrier gas, respectively. The fourth term, $k_Q[Q]$ is the timescale associated with the de-excitation of the metastable state with an added reagent; this is the rate which will dominate the de-excitation of metastable Kr atoms in typical fluid mechanics applications of interest to the aerothermodynamics community.

If we assume a fluorescence signal towards the high side of the 16-bit camera's dynamic range at the write location (which is possible with the current experimental setup), then the number of recordable metastable lifetimes is estimated as $2^{16} \approx \exp(-t/\tau_m)$. We take $\ln(2^{16}) \approx 10 = t/\tau_m$ which leads to the estimation that we can record the displacement of metastable Kr for approximately 10 lifetimes.

In Table 3.1, we list the relevant parameters for KTV measurement; namely, local density, $\rho_\infty$, and the length scale, $x_m$. The length scale, $x_m$, is computed as the product of the timescale from Eq. 4.1, the local velocity scale, $U_\infty$, and a factor of 10 to account for the 10 metastable lifetimes that are recorded as $x_m \approx 10\tau_m U_\infty$.

We note that in Table 3.1, the estimated lifetime of the metastable tracer is

approximately the same for the Mach 3 AEDC Calibration Tunnel and AEDC Tunnel 9. This means that experiments in the Mach 3 AEDC Calibration Tunnel are a good simulation of future Tunnel 9 experiments. For-longer term goals, we plan to use KTV to measure the velocity profiles over flight-vehicle models in AEDC Tunnel 9 and high-enthalpy impulse facilities like Caltech's T5 reflected shock tunnel.[55] The useful length scale for each of these facilities was derived from Marineau et al.[56] (Tunnel 9) and Parziale et al.[44] (T5). In Table 3.1, it is seen that the metastable lifetime ($\tau_m$) and the displacement distance ($x_m$) to be are estimated to be sufficient as to permit KTV measurements in Tunnel 9 or T5.

### 4.3 Krypton Gas Bottle Cost

Krypton gas-bottle cost is appropriate for laboratory-scale KTV efforts. In this work, we performed approximately ≈100 experiments with approximately ≈4k USD worth of pre-mixed research grade krypton, yielding a ≈40 USD per experiment cost. We initially estimated that the seeding cost per run of 1% Kr mole fraction ranges from ≈10 USD in impulse facilities (e.g, Ludwieg Tubes, shocktunnels, and moderate reservoir pressure blow-down facilities) to ≈50-500 USD in high reservoir pressure long-duration blow-down hypersonic tunnels (e.g., Tunnel 9 at AEDC White Oak[47]). The range of cost is dependent on the unit Reynolds number (through local number density) the facility is to be run operated at; for the Tunnel 9 condition listed in Table 3.1 ($\mathrm{Re}_\infty^{unit}$ = 15e6 1/m), the estimated cost is ≈200 USD which is a small fraction of large-scale tunnel operation costs.

## 4.4 Supersonic Turbulent Boundary Layer Results

In this chapter, we present KTV and Pitot-derived velocity profiles of the turbulent boundary layer on the wall of the AEDC White Oak Mach 3 Calibration Tunnel. The freestream was comprised of 99% $N_2$/1% Kr at momentum-thickness Reynolds numbers of $\mathrm{Re}_\Theta = \rho_e U_e \Theta/\mu_e$ = 800, 1400, and 2400. The momentum thickness is defined as

$$\Theta = \int_0^\infty \frac{\rho}{\rho_e}\frac{U}{U_e}\left(1-\frac{U}{U_e}\right)dy. \tag{4.2}$$

Pitot-derived velocity profiles were made at discrete wall-normal distances with Pitot and static pressure measurement using the same methodology as Brooks et al.[57,58] The Mach number was found with the Rayleigh-Pitot probe formula (Eq. 3.4).[50] The local temperature was found using Walz's[59] relation

$$\frac{T}{T_e} = \frac{T_w}{T_e} + \frac{T_r - T_w}{T_e}\left(\frac{U}{U_e}\right) - r\frac{\gamma-1}{2}M_e^2\left(\frac{U}{U_e}\right)^2 \tag{4.3}$$

with the recovery temperature $T_r$ is defined as

$$\frac{T_r}{T_e} = 1 + r\frac{\gamma-1}{2}M_e^2. \tag{4.4}$$

KTV measurements were performed by tracking the tagged Kr center-of-mass locations for a prescribed time. Example exposures that illustrate the unsteady nature of the supersonic turbulent boundary layer are presented as Fig. 4.2. Each exposure is processed with a 3 pixel x 3 pixel ($\approx$ 291 µm x 291 µm) two-dimensional Wiener adaptive-noise removal filter in MATLAB. Then, a Gaussian model of the form $f(x) = a\exp\left(-((x-b)/c)^2\right)$ is fitted to the intensity vector for each exposure

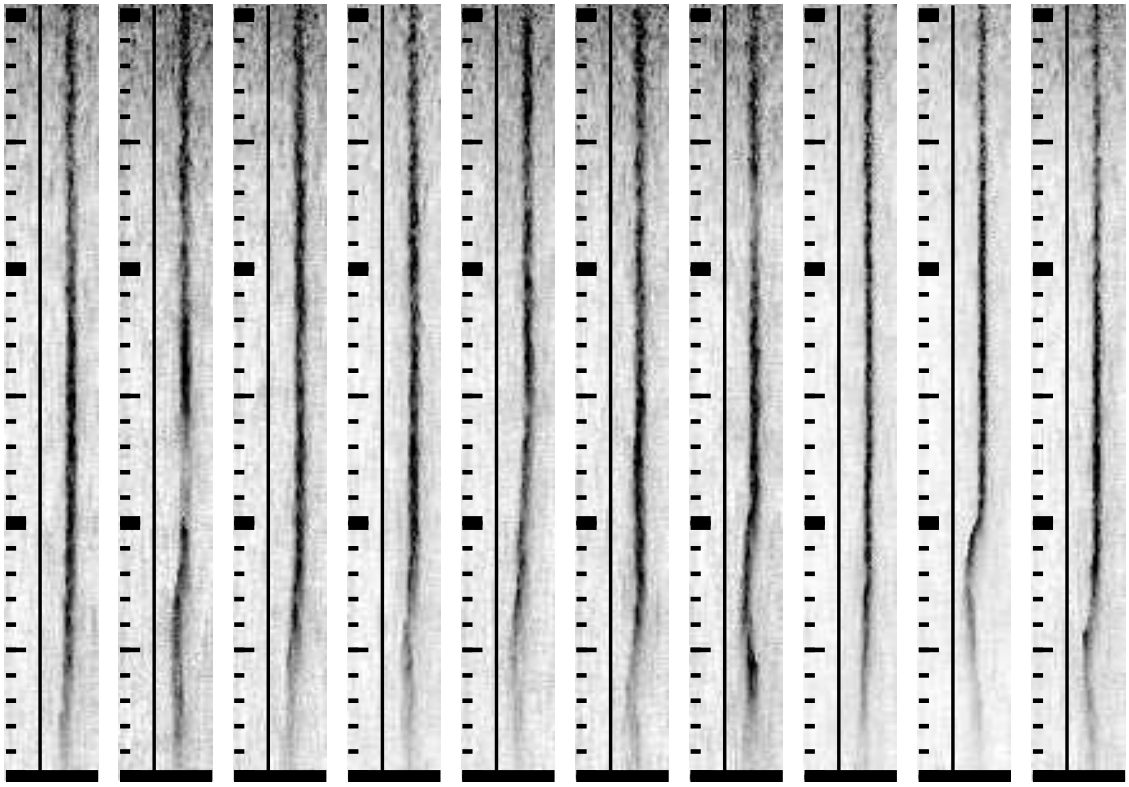

Figure 4.2: KTV in a 99% $N_2$/1% Kr Mach 2.75 turbulent boundary layer with a $Re_\Theta$=800. Flow is left to right. Inverted intensity scale. The write location is marked by a vertical, thin black line. The camera gate is fixed to include only the read laser pulses. The delay between the write and read lines is 2 µs. Major tick marks at 10 mm intervals.

in the x-direction for each row of pixels in the wall-normal direction ($\approx$ 97 µm wall-normal direction x 5.0 mm streamwise direction). The centroid ($b$) and the 95% confidence bounds are determined with the non-linear least squares method. The streamwise displacement distance, $\Delta x$, is then found as the read-centroid location relative to the write-centroid location. The local velocity is found as $U = \Delta x/\Delta t$, where $\Delta t$ is prescribed by a pulse/delay generator as $\Delta t = 2$ µs.

We present the dimensional velocity profiles for three conditions with $Re_\Theta$=800 (Fig. 4.3(a)), $Re_\Theta$=1400 (Fig. 4.3(b)), and $Re_\Theta$=2400 (Fig. 4.3(c)). The KTV results are reported along with Pitot-tube derived velocity measurements and predicted tur-

bulent profiles from the Virginia Tech (VT) Compressible Turbulent Boundary Layer applet from Devenport and Schetz.[60,61]

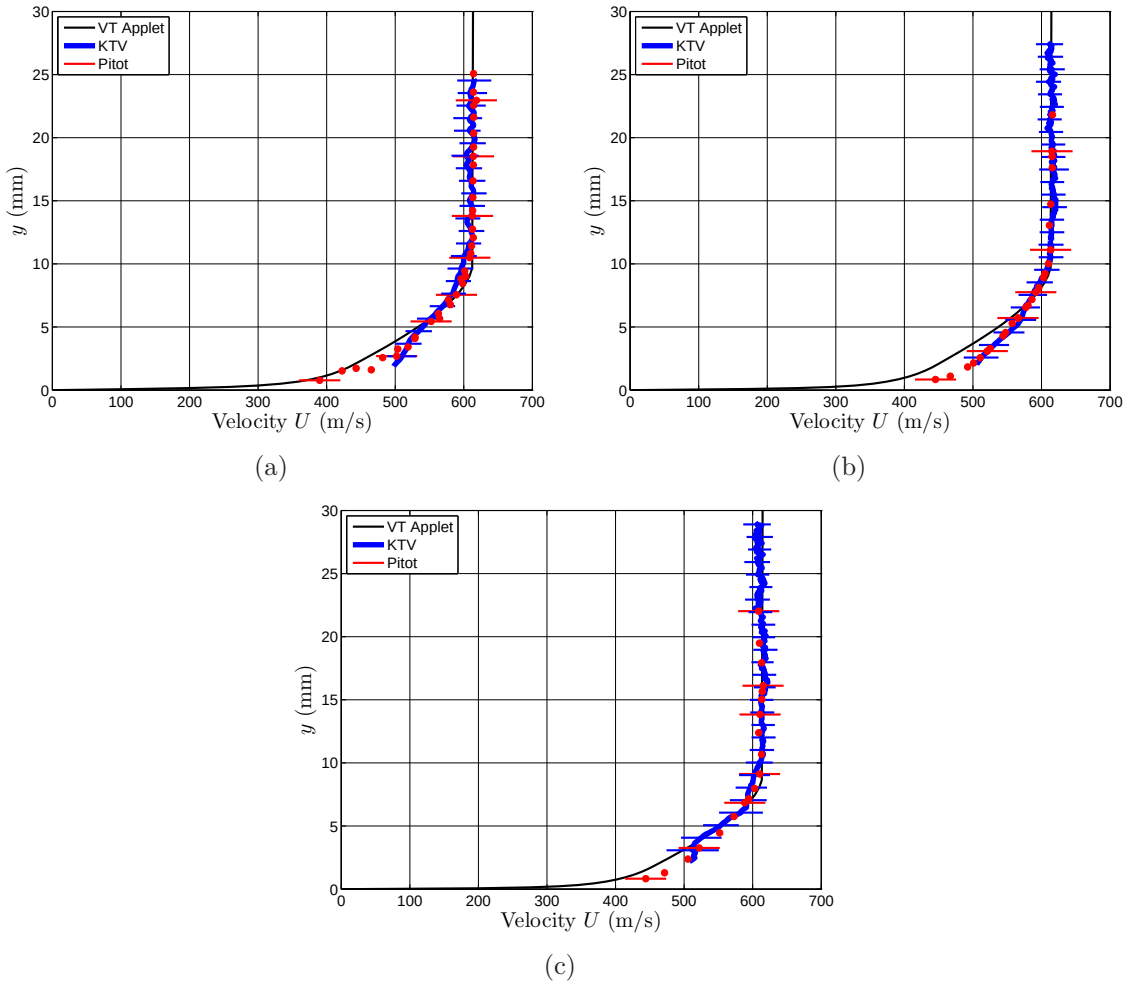


Figure 4.3: Profiles in a 99% $N_2$/1% Kr Mach 2.75 turbulent boundary layer with $Re_\Theta$=800 (a), $Re_\Theta$=1400 (b), and $Re_\Theta$=2400 (c).

For each case, $Re_\Theta$ = 800, 1400, 2400, agreement between the three mean velocity profiles (KTV, Pitot, and VT Applet) is good, particularly between the Pitot and KTV measurements. The small discrepancy between the VT applet and the measurements may be attributed to assumptions that go into the VT applet: it is assumed that there is no pressure history (flat plate) and the transition occurs at the nozzle throat. Boundary-layer trips were placed near the throat; however,

particularly for the $\mathrm{Re}_\Theta = 800$ case, the Reynolds number may not be sufficient to result in an equilibrium turbulent boundary layer at the measurement location which was $\approx 500$ mm from the throat. KTV results near the windtunnel wall ($y/\delta_{99} < 0.1$) are not reported because the Gaussian fits to the read data were found to be unreliable. The lack of repeatable results close to the windtunnel wall ($y/\delta_{99} < 0.1$) is likely due to the high levels of fluctuation which smear the KTV tracer, yielding low SNR from the read pulse. Further study is required to confirm this.

Uncertainty in the velocimetry data was estimated following Moffat.[62] For the Pitot-derived velocity data, we assume that the uncertainty is determined by the reservoir temperature, Pitot pressure, and static pressure as

$$\delta U_{\mathrm{Pitot}} = \left[ \left( \delta P_{02} \frac{\partial U}{\partial P_{02}} \right)^2 + \left( \delta P_\infty \frac{\partial U}{\partial P_\infty} \right)^2 + \left( \delta T_\infty \frac{\partial U}{\partial T_\infty} \right)^2 \right]^{\frac{1}{2}}. \tag{4.5}$$

The uncertainty in Pitot-derived velocity from the Pitot pressure and static pressure can be determined using the Rayleigh-Pitot Probe Formula (Eq. 3.4). The uncertainty in the pressure transducer response is from comparisons of in-house calibrations against high-accuracy Baratron pressure transducers. The uncertainty in Pitot-derived velocity from the reservoir temperature is determined using the sound speed and the measured unsteadiness during the test time (Fig. 3.7(a)).

For the KTV-derived velocity data, we assume that the uncertainty is determined by the uncertainty in the measured displacement distance of the metastable tracer and the timing accuracy of the experiment as

$$\delta U_{\mathrm{KTV}} = \left[ \left( \delta \Delta x \frac{\partial U}{\partial \Delta x} \right)^2 + \left( \delta \Delta t \frac{\partial U}{\partial \Delta t} \right)^2 \right]^{\frac{1}{2}}. \tag{4.6}$$

The uncertainty in the measured displacement distance, $\Delta x$, of the metastable tracer is estimated as the 95% confidence bound on the write and read locations. The uncertainty $\Delta t$ is estimated to be 50 ns, primarily due to fluorescence blurring as considered in Bathel et al.[63] From the manufacturerŠs specification, we estimate that the jitter is relatively small, approximately 1 ns for each laser. The fluorescence blurring primarily occurs because of the time scale associated with the 819.0 nm $5p[3/2]_2 \rightarrow 5s[3/2]_1^o$ transition (25 ns);[64–67] so, we double this value and report that as the uncertainty in $\Delta t$.

### 4.5 Analysis

In this chapter, the velocity profiles in Fig. 4.3 are non-dimensionalized to analyze the KTV and Pitot data in the logarithmic and outer region of the boundary layer. The shear velocity, $u_\tau = \sqrt{\tau_w/\rho_w}$, is required and the method of calculation can be found from Eq. A.1 in Appendix A.

The velocity data from the present study can be compared to the log law, $U^+ = 1/0.41\mathrm{Ln}(y^+) + 5.2$, by using the Van Driest I transformation, with $y^+ = \rho_w u_\tau u/\mu_w$ and $U^+ = U/u_\tau$. Following, Huang and Coleman[68] and Bradshaw,[69] the Van Driest transformed velocity can be written as

$$U_{VD}^+ = \left[\sin^{-1}\left(\frac{R(U^+ + H)}{\sqrt{1+R^2H^2}}\right) - \sin^{-1}\left(\frac{RH}{\sqrt{1+R^2H^2}}\right)\right]/R, \tag{4.7}$$

where $R = M_\tau\sqrt{(\gamma-1)\,\mathrm{Pr}_t\,/2}$, $H = B_q/((\gamma-1)M_\tau^2)$, $M_\tau = u_\tau/c_w$, and $B_q = q_w/(\rho_w c_p u_\tau T_w)$. We assume the turbulent Prandtl number is $\mathrm{Pr}_t = 0.87$, and, assuming the Reynolds analogy holds, the heat-flux number is $B_q = c_f\rho_e U_e(T_w - T_r)/(2\,\mathrm{Pr}_e\,\rho_w u_\tau T_w)$.[70] The transformed KTV- and Pitot-derived velocity profiles

are presented in Fig. 4.4(a). Also, in Fig. 4.4(a), we plot $U_{VD}^{+} = y^{+}$ and $U_{VD}^{+} = 1/0.41\mathrm{Ln}(y^{+}) + 5.2$. The transformed velocity follows the law of the wall in the logarithmic-law region with good agreement.

Fernholtz and Finley[71–73] outline a velocity-defect law to scale the outer layer of the turbulent boundary layer. In their work, Fernholtz and Finley define an integral length scale as

$$\Delta^{*} = \int_{0}^{\infty} \frac{U_{e}^{*} - \bar{U}^{*}}{u_{\tau}} dy \tag{4.8}$$

where $U_{e}^{*}$ and $\bar{U}^{*}$ are the edge and local mean velocities defined by

$$U^{*} = \frac{U_{e}}{b} \sin^{-1} \frac{2b^{2}U/U_{e} - a}{\sqrt{a^{2} + 4b^{2}}} \tag{4.9}$$

and $a$ and $b$ are defined as

$$a = \frac{T_{e}}{T_{w}} \left(1 + r\frac{\gamma - 1}{2} M_{e}^{2}\right) - 1 \tag{4.10}$$

$$b^{2} = \frac{T_{e}}{T_{w}} \left(r\frac{\gamma - 1}{2} M_{e}^{2}\right). \tag{4.11}$$

The resulting non-dimensional profiles are presented as Fig. 4.4(b). The scaling collapses the profiles satisfactorily. Also in Fig. 4.4(b), we plot $(U_{e}^{*} - \bar{U}^{*})/(u_{\tau}) = -M\mathrm{Ln}(y/\Delta^{*}) - N$, with $M = 4.7, N = 6.74$. Here, $M$ is not the Mach number but a constant that is consistent with the nomenclature of Fernholtz and Finley, where they propose the $(U_{e}^{*} - \bar{U}^{*})/(u_{\tau}) = -4.7\mathrm{Ln}(y/\Delta^{*}) - 6.74$ relation for a turbulent boundary layer with zero pressure gradient. The agreement between the transformed KTV and Pitot velocity and $(U_{e}^{*} - \bar{U}^{*})/(u_{\tau}) = -4.7\mathrm{Ln}(y/\Delta^{*}) - 6.74$ is poor. Values of $\mathrm{Ln}(y/\Delta^{*}) > -1.5$ at the boundary-layer edge ($(U_{e}^{*} - \bar{U}^{*})/(u_{\tau}) = 0$), are consistent

with data from the literature with a favorable pressure gradient.[71–73]

The RMS streamwise-velocity fluctuations, $u'_{rms}$, as measured by KTV and non-dimensionalized by the edge velocity are presented in Fig. 4.5(a). The KTV fluctuation measurements collapse for each case, except for the $Re_\Theta = 800$ case outside of the boundary layer. The reason for this raised level of fluctuation outside the boundary layer is unknown at the time of this writing.

The Morkovin[74] scaling ($\sqrt{\rho}u'_{rms}/\sqrt{\rho_w}u_\tau$) is applied to the data and presented in Fig. 4.5(b). In that figure, we overlay data from the literature from hot-wire anemometry (HWA) measurements from Klebanoff[75] recorded in a low-speed boundary layer (30 ft/s) and HWA and one- and two-component LDV measurements in a $M_e = 2.3$, $Re_\Theta = 4700$ boundary layer from Elena et al.[76] These data are also compared to DNS data in a $M_e = 2.3$, $Re_\Theta = 4450$ boundary layer from Martin.[77] The agreement between the KTV data from this work and the experimental and

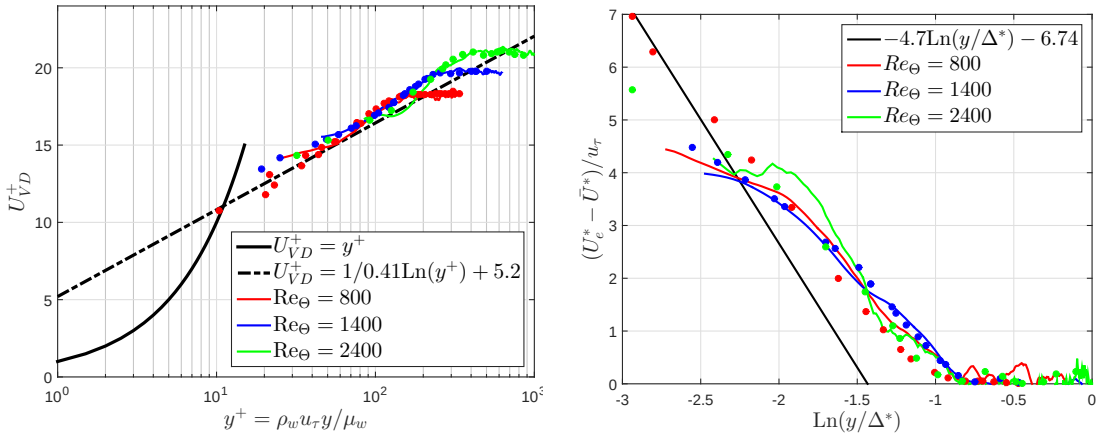


(a) (b)

Figure 4.4: Non-dimensional velocimetry data for profiles in a 99% $N_2$/1% Kr Mach 2.75 turbulent boundary layer with $\mathrm{Re}_\Theta$=800,1400, 2400. Dots are Pitot-derived velocity. Lines are KTV-derived velocity. (a): Comparison of the Van Driest transformed velocity to the log law. (b): Velocity-defect law scaling of turbulent boundary layer.

computational data is good for wall-normal distances $y/\delta_{99} > 0.2$.

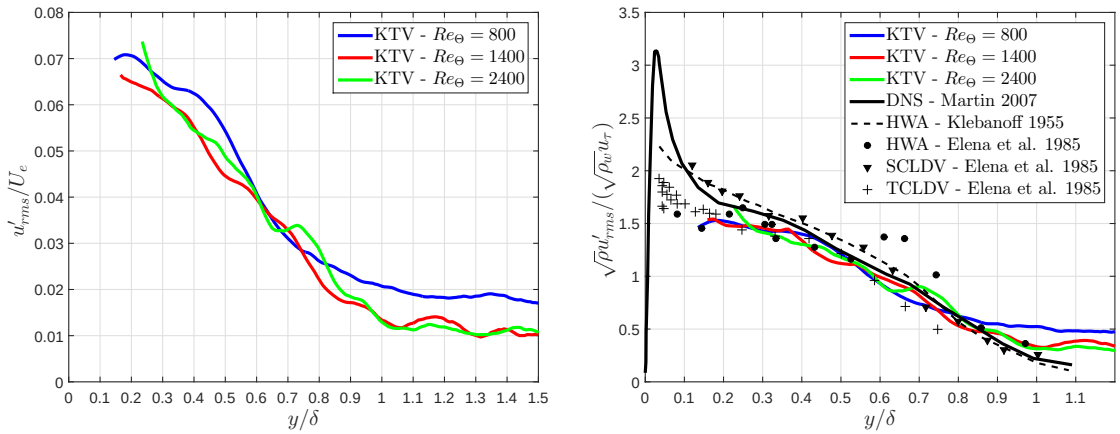


(a) (b)

Figure 4.5: Streamwise-velocity fluctuation KTV data non-dimensionalized by the edge velocity in (a) and the Morkovin scaling in (b). and compared to historical data from Klebanoff[75] from an low-speed tunnel, Elena et al.[76]from a $M_e = 2.3$, $Re_\Theta = 4700$ boundary layer by hot-wire anemometry (HWA) and one- and two-component laser-Doppler velocimetry (LVD). These data are compared to direct numerical simulation (DNS) from Martin[77] from a $M_e = 2.3$, $Re_\Theta = 4450$ boundary layer.

# Chapter 5

## Conclusions and Future Work

To assess the potential use of the KTV technique to AEDC Hypervelocity Tunnel 9, the Mach 3 AEDC Calibration Tunnel was modified so that the unit Reynolds number could be prescribed at several values consistent with AEDC Tunnel 9 run conditions. The modification was comprised of an orifice plate, PVC pipe, and three perforated screens. These components were used to isothermally reduce the reservoir pressure, and thus the freestream unit Reynolds number.

In this work, we highlight the KTV measurement of a Mach 2.75 turbulent boundary layer at momentum thickness Reynolds numbers of $\mathrm{Re}_\Theta = 800$, 1400, and 2400. Pitot-derived velocity data was also taken for the flowfield, and agreement between the KTV- and Pitot-derived velocity profiles is good. Moreover, the experimental profiles of velocity (both KTV and Pitot) agree with the predicted profiles from the Virginia Tech (VT) Compressible Turbulent Boundary Layer applet from Devenport and Schetz.[60,61]

The KTV- and Pitot-derived profiles of velocity are compared to the law of the wall with the application of the Van Driest I transformation, and agreement in the logarithmic-law region is good. From this, we conclude that KTV may be used to measure profiles of velocity in the logarithmic law region of turbulent boundary layers.

The data is also scaled according to the velocity-defect law outlined in Fernholtz and Finley,[71–73] and the KTV and Pitot profiles collapse for the data taken at $Re_\Theta$=800, 1400 and 2400. The KTV and Pitot data do not follow the scaling reported

by Fernholtz and Finley of $(U_e^* - \bar{U}^*)/(u_\tau) = -4.7\log(y/\Delta^*) - 6.74$. Near the abscissa of Fig. 4.4(b), in the wake region, the present data fall $\mathrm{Ln}(y/\Delta^+) > 1.5$. Fernholtz and Finely propose their parameters for the Reynolds number range $1500 < Re_{\delta 2} < 40000$ with zero pressure gradient. Here, $Re_{\delta 2} = \rho_e U_e \Theta/\mu_w$, and in this work, $Re_\Theta$=800, 1400 and 2400 corresponds to $Re_{\delta 2}$= 350, 625, and 1100, respectively. Fernholtz and Finley assert that the agreement with the values $M = 4.7$ and $N = 6.74$ improves with increasing Reynolds number. The deviation from the scaling of the data from the present work in the outer region from the proposed form may be due to the low Reynolds number; however, the favorable pressure gradient history from the nozzle expansion in the present work may also play a role. For example, the data of Lewis et al.[78] characterize a compressible turbulent boundary layer with favorable and adverse pressure gradients. The Lewis et al. data from a favorable pressure gradient case is recast in Fernholtz and Finley[72] as Fig. 5.2.2. The Lewis et al. data show an offset to the right of $\mathrm{Ln}(y/\Delta^+) \approx 1.5$ near the abscissa (in the wake region) that is similar to the offset of the data presented in this work. Juxtaposed to this is the offset to the left of $\mathrm{Ln}(y/\Delta^+) \approx 1.5$ near the abscissa for an adverse pressure gradient in Fig. 5.3.5 of Fernholtz and Finley.[72] That is, the data in the present work is consistent with data from the literature for a favorable pressure gradient. From this, we conclude that KTV may be used to assess some fundamental characteristics of compressible turbulent boundary layers, such as pressure gradient history.

The KTV technique is used to quantify the streamwise-velocity fluctuations. The KTV fluctuation measurements collapse for each case, except for the $Re_\Theta = 800$ case outside of the boundary layer. The reason for this raised level of fluctuation outside the boundary layer is not clear at the time of this writing. The Morkovin scaling is applied to the RMS fluctuation data. The agreement between the computational

and experimental data from the literature and KTV measurements from this work is good for wall-normal distances $y/\delta_{99} > 0.2$. Measurements below $y/\delta_{99} \approx 0.1 - 0.2$ are difficult to perform, and the issue in doing so with KTV may be that the tracer is smeared out because of the increase in velocity fluctuations near the wall (Fig. 4.5(b)). In the future, it may be possible to resolve the near-wall fluctuations by reducing the time between the write and read laser pulses so as to reduce the turbulent diffusion of the metastable Kr tracer.

# Appendix A

## Appendix A - Calculation of Skin Friction and Shear Velocity

To determine the shear velocity, $u_\tau = \sqrt{\tau_w/\rho_w}$, the shear stress at the wall, $\tau_w$, must be determined. Following Xu and Martin,[79] the skin friction coefficient, $c_f = \tau_w/(0.5\rho_e U_e^2)$, can be determined from the Kármán[80]-Schoenherr[81] equation under the Van Driest II transformation as

$$\frac{1}{c_f F_c} = 17.08\left(\log_{10}(F_\Theta Re_\Theta)\right)^2 + 25.11\log_{10}(F_\Theta Re_\Theta) + 6.012 \tag{A.1}$$

where

$$F_c = 0.2rM_e^2/(\sin^{-1}(\alpha) + \sin^{-1}(\beta))^2 \tag{A.2}$$

$$F_\Theta = \mu_e/\mu_w, \tag{A.3}$$

and $r = 0.9$ is the recovery factor. The parameters $\alpha$ and $\beta$ are computed as

$$\alpha = (2A^2 - B)/\sqrt{4A^2 + B^2} \tag{A.4}$$

$$\beta = B/\sqrt{4A^2 + B^2} \tag{A.5}$$

with

$$A^2 = 0.2rM_e^2/(T_w/T_e) \tag{A.6}$$

$$B = (1 + 0.2rM_e^2 - T_w/T_e)/(T_w/T_e). \tag{A.7}$$

## Bibliography

[1] V. J. Bilardo, F. M. Curran, J. L. Hunt, N. T. Lovell, G. Maggio, A. W. Wilhite, and L. E. McKinney. The Benefits of Hypersonic Airbreathing Launch Systems for Access to Space. In *Proceedings of 39TH AIAA/ASME/SAE/ASEE Joint Propulsion Conference and Exhibit*, Huntsville, Alabama, 2003. AIAA-2003-5265. doi: 10.2514/6.2003-5265.

[2] A. F. Woolf. Conventional Prompt Global Strike and Long-Range Ballistic Missiles: Background and Issues. R41464, 2014. Congressional Research Service.

[3] A. G. Panaras. *Aerodynamic Principles of Flight Vehicles*. American Institute of Aeronautics and Astronautics, 2012.

[4] J. J. Bertin. *Hypersonic Aerothermodynamics*. American Institute of Aeronautics and Astronautics, 1994.

[5] E.T. Curran. The Potential and Practicality of High Speed Combined Cycle Engines. In *Conference Proceedings No. 479*. Advisory Group for Aerospace Research and Development (AGARD), NATO, 1990.

[6] J.V. Becker. New Approaches to Hypersonic Aircraft. In *Seventh Congress of the International Council of the Aeronautical Sciences*, Rome, Italy, 1970.

[7] G. V. Candler. Rate-dependent energetic processes in hypersonic flows. *Progress in Aerospace Sciences*, 72:37–48, 2015. doi: 10.1016/j.paerosci.2014.09.006.

[8] T. E. Schwartzentruber and I. D. Boyd. Progress and Future Prospects for Particle-Based Simulation of Hypersonic Flow. *Progress in Aerospace Sciences*,

72:66–79, 2015. doi: 10.1016/j.paerosci.2014.09.003.

[9] D. Bose, J. L. Brown, D. K. Prabhu, P. Gnoffo, C. O. Johnston, and B. Hollis. Uncertainty Assessment of Hypersonic Aerothermodynamics Prediction Capability. *Journal of Spacecraft and Rockets*, 50(1):12–18, 2013. doi: 10.2514/1.A32268.

[10] D. Marren, M. Lewis, and L. Q. Maurice. Experimentation, Test, and Evaluation Requirements for Future Airbreathing Hypersonic Systems. *Journal of Propulsion and Power*, 17(6):1361–1365, 2001. doi: 10.2514/2.5888.

[11] B. McKeon, G. Comte-Bellot, J. Foss, J. Westerweel, F. Scarano, C. Tropea, J. Meyers, J. Lee, A. Cavone, R. Schodl, M. Koochesfahani, Y. Andreopoulos, W. Dahm, J. Mullin, J. Wallace, P. VukoslavÄĐeviÄĞ, S. Morris, E. Pardyjak, and A. Cuerva. Velocity, Vorticity, and Mach Number. In Tropea, C. and Yarin, A. L. and Foss, J. F., editor, *Springer Handbook of Experimental Fluid Mechanics*, pages 215–471. Springer, 2007.

[12] A. H.. Meier and T Roesgen. Imaging laser doppler velocimetry. *Experiments in Fluids*, 52(4):1017–1026, 2012. doi: 10.1007/s00348-011-1192-1.

[13] A. H.. Meier and T. Roesgen. Heterodyne doppler global velocimetry. *Experiments in Fluids*, 47(4-5):665–672, 2009. doi: 10.1007/s00348-009-0647-0.

[14] M.S. Maurice. Particle size distribution technique using conventional laser doppler velocimetry measurements. *AIAA journal*, 34(6):1209–1215, 1996.

[15] J. Haertig, M. Havermann, C. Rey, and A. George. Particle Image Velocimetry in Mach 3.5 and 4.5 Shock-Tunnel Flows. *AIAA Journal*, 40(6):1056–1060, 2002. doi: 10.2514/2.1787.

[16] Koochesfahani, M. M. and Nocera, D. G. Molecular Tagging Velocimetry. In *Springer Handbook of Experimental Fluid Mechanics*. Springer, 2007.

[17] A. G. Hsu, R. Srinivasan, R. D. W. Bowersox, and S. W. North. Molecular Tagging Using Vibrationally Excited Nitric Oxide in an Underexpanded Jet Flowfield. *AIAA Journal*, 47(11):2597–2604, 2009. doi: 10.2514/1.39998.

[18] A. G. Hsu, R. Srinivasan, R. D. W. Bowersox, and S. W. North. Two-Component Molecular Tagging Velocimetry Utilizing NO Fluorescence Lifetime and $NO_2$ Photodissociation Techniques in an Underexpanded Jet Flowfield. *Applied Optics*, 48(22):4414–4423, 2009. doi: 10.1364/AO.48.004414.

[19] R. Sánchez-González, R. Srinivasan, R. D. W. Bowersox, and S. W. North. Simultaneous velocity and temperature measurements in gaseous flow fields using the venom technique. *Optics Letters*, 36(2):196–198, 2011. doi: 10.1364/OL.36.000196.

[20] R. Sánchez-González, R. D. W. Bowersox, and S. W. North. Simultaneous velocity and temperature measurements in gaseous flowfields using the vibrationally excited nitric oxide monitoring technique: a comprehensive study. *Applied Optics*, 51(9):1216–1228, 2012. doi: 10.1364/AO.51.001216.

[21] R. Sánchez-González, R. D. W. Bowersox, and S. W. North. Vibrationally Excited NO Tagging by $NO(A^2\Sigma^+)$ Fluorescence and Quenching for Simultaneous Velocimetry and Thermometry in Gaseous Flows. *Optics Letters*, 39(9):2771–2774, 2014. doi: 10.1364/OL.39.002771.

[22] N. Dam, R. J. H. Klein-Douwel, N. M. Sijtsema, and J. J. ter Meulen. Nitric oxide flow tagging in unseeded air. *Optics Letters*, 26(1):36–38, 2001. doi: 10.1364/OL.26.000036.

[23] N. M. Sijtsema, N. J. Dam, R. J. H. Klein-Douwel, and J. J. ter Meulen. Air Photolysis and Recombination Tracking: A New Molecular Tagging Velocimetry Scheme. *AIAA Journal*, 40(6):1061–1064, 2002. doi: 10.2514/2.1788.

[24] W. P. N. Van der Laan, R. A. L. Tolboom, N. J. Dam, and J. J. ter Meulen. Molecular tagging velocimetry in the wake of an object in supersonic flow. *Experiments in Fluids*, 34(4):531–534, 2003. doi: 10.1007/s00348-003-0593-1.

[25] R. Miles, C. Cohen, J. Connors, P. Howard, S. Huang, E. Markovitz, and G. Russell. Velocity measurements by vibrational tagging and fluorescent probing of oxygen. *Optics Letters*, 12(11):861–863, 1987. doi: 10.1364/OL.12.000861.

[26] R.B. Miles, J.J. Connors, E.C. Markovitz, P.J. Howard, and G.J. Roth. Instantaneous Profiles and Turbulence Statistics of Supersonic Free Shear Layers by Raman Excitation Plus Laser-Induced Electronic Fluorescence (RELIEF) Velocity Tagging of Oxygen. *Experiments in Fluids*, 8(1-2):17–24, 1989. doi: 10.1007/BF00203060.

[27] R. B. Miles, D. Zhou, B. Zhang, and W. R. Lempert. Fundamental Turbulence Measurements by RELIEF Flow Tagging. *AIAA Journal*, 31(3):447–452, 1993. doi: 10.2514/3.11350.

[28] R. B. Miles and W. R. Lempert. Quantitative Flow Visualization in Unseeded Flows. *Annual Review of Fluid Mechanics*, 29(1):285–326, 1997. doi: 10.1146/annurev.fluid.29.1.285.

[29] R. B. Miles, J. Grinstead, R. H. Kohl, and G. Diskin. The RELIEF Flow Tagging Technique and its Application in Engine Testing Facilities and for Helium-Air Mixing Studies. *Measurement Science and Technology*, 11(9):1272–1281, 2000. doi: 10.1088/0957-0233/11/9/304.

[30] J. C. McDaniel, B. Hiller, and R. K. Hanson. Simultaneous multiple-point velocity measurements using laser-induced iodine fluorescence. *Optics Letters*, 8(1):51–53, 1983. doi: 10.1364/OL.8.000051.

[31] R. J. Balla. Iodine Tagging Velocimetry in a Mach 10 Wake. *AIAA Journal*, 51(7):1–3, 2013. doi: 10.2514/1.J052416.

[32] W. R. Lempert, N. Jiang, S. Sethuram, and M. Samimy. Molecular Tagging Velocimetry Measurements in Supersonic Microjets. *AIAA Journal*, 40(6):1065–1070, 2002. doi: 10.2514/2.1789.

[33] W. R. Lempert, M. Boehm, N. Jiang, S. Gimelshein, and D. Levin. Comparison of molecular tagging velocimetry data and direct simulation monte carlo simulations in supersonic micro jet flows. *Experiments in Fluids*, 34(3):403–411, 2003. doi: 10.1007/s00348-002-0576-7.

[34] T. Handa, K. Mii, T. Sakurai, K. Imamura, S. Mizuta, and Y. Ando. Study on supersonic rectangular microjets using molecular tagging velocimetry. *Experiments in Fluids*, 55(5):1–9, 2014. doi: 10.1007/s00348-014-1725-5.

[35] L. R. Boedeker. Velocity Measurement by $H_2O$ Photolysis and Laser-Induced Fluorescence of OH. *Optics Letters*, 14(10):473–475, 1989. doi: 10.1364/OL.14.000473.

[36] J. A. Wehrmeyer, L. A. Ribarov, D. A. Oguss, and R. W. Pitz. Flame Flow Tagging Velocimetry with 193-nm $H_2O$ Photodissociation. *Applied Optics*, 38(33):6912–6917, 1999. doi: 10.1364/AO.38.006912.

[37] R. W. Pitz, M. D. Lahr, Z. W. Douglas, J. A. Wehrmeyer, S. Hu, C. D. Carter, K.-Y. Hsu, C. Lum, and M. M. Koochesfahani. Hydroxyl tagging velocime-

try in a supersonic flow over a cavity. *Applied Optics*, 44(31):6692–6700, 2005. doi: 10.1364/AO.44.006692.

[38] B. Hiller, R. A. Booman, C. Hassa, and R. K. Hanson. Velocity visualization in gas flows using laser-induced phosphorescence of biacetyl. *Review of Scientific Instruments*, 55(12):1964–1967, 1984. doi: 10.1063/1.1137687.

[39] C. P. Gendrich and M. M. Koochesfahani. A Spatial Correlation Technique for Estimating Velocity Fields Using Molecular Tagging Velocimetry (MTV). *Experiments in Fluids*, 22(1):67–77, 1996. doi: Springer.

[40] C. P. Gendrich, M. M. Koochesfahani, and D. G. Nocera. Molecular tagging velocimetry and other novel applications of a new phosphorescent supramolecule. *Experiments in Fluids*, 23(5):361–372, 1997. doi: 10.1007/s003480050123.

[41] B. Stier and M. M. Koochesfahani. Molecular Tagging Velocimetry (MTV) Measurements in Gas Phase Flows. *Experiments in Fluids*, 26(4):297–304, 1999. doi: 10.1007/s003480050292.

[42] J. F. Lafferty and D. E. Marren. Hypervelocity wind tunnel no. 9 mach 7 thermal structural facility verification and calibration. NSWCDD/TR-95/231, 1996.

[43] N. J. Parziale, M. S. Smith, and E. C. Marineau. Krypton Tagging Velocimetry for Use in High-Speed Ground-Test Facilities. In *Proceedings of AIAA SciTech 2015*, Kissimmee, Florida, 2015. AIAA-2015-1484. doi: 10.2514/6.2015-1484.

[44] N. J. Parziale, M. S. Smith, and E. C. Marineau. Krypton Tagging Velocimetry of an Underexpanded Jet. *Applied Optics*, 54(16):5094–5101, 2015. doi: 10.1364/AO.54.005094.

[45] J. L. Mills, C. I. Sukenik, and R. J. Balla. Hypersonic Wake Diagnostics Using Laser Induced Fluorescence Techniques. In *Proceedings of 42nd AIAA Plasmadynamics and Lasers Conference*, Honolulu, Hawaii, 2011. AIAA 2011-3459. doi: 10.2514/6.2011-3459.

[46] R. J. Balla and J. L. Everhart. Rayleigh Scattering Density Measurements, Cluster Theory, and Nucleation Calculations at Mach 10. *AIAA Journal*, 50(3):698–707, 2012. doi: 10.2514/1.J051334.

[47] Marren, D. and Lafferty, J. The AEDC Hypervelocity Wind Tunnel 9. In *Advanced Hypersonic Test Facilities*, pages 467–478. American Institute of Aeronautics and Astronautics, 2002. doi: 10.2514/5.9781600866678.0467.0478.

[48] A. C. Eckbreth. *Laser Diagnostics for Combustion Temperature and Species*. Gordon and Breach Publications, second edition, 1996.

[49] F. White. *Fluid Mechanics*. McGraw-Hill Education, 2015.

[50] H. W. Liepmann and A. Roshko. *Elements of Gasdynamics*. John Wiley and Sons, Inc., 1957.

[51] C. J. Tracy and H.J. Oskam. Properties of Metastable Krypton Atoms in Afterglows Produced in Krypton and Krypton–Nitrogen Mixtures. *The Journal of Chemical Physics*, 65(5):1666–1671, 1976. doi: 10.1063/1.433312.

[52] J. E. Velazco, J. H. Kolts, and D. W. Setser. Rate Constants and Quenching Mechanisms for the Metastable States of Argon, Krypton, and Xenon. *The Journal of Chemical Physics*, 69(10):4357–4373, 1978. doi: 10.1063/1.436447.

[53] R. Sobczynski and D. W. Setser. Improvements in the Generation and Detection of $Kr(^3P_0)$ and $Kr(^3P_2)$ Atoms in a Flow Reactor: Decay Constants in He Buffer

and Total Quenching Rate Constants for Xe, $N_2$, CO, $H_2$, $CF_4$, and $CH_4$. *The Journal of Chemical Physics*, 95(5):3310–3324, 1991. doi: 10.1063/1.460837.

[54] D. A. Zayarnyi, A. Yu L'dov, and I. V. Kholin. Deactivation of Krypton Atoms in the Metastable $5s(^3P_2)$ State in Collisions with Krypton and Argon Atoms. *Quantum Electronics*, 39(9):821, 2009. doi: 10.1070/QE2009v039n09ABEH013999.

[55] H. G. Hornung. Experimental Hypervelocity Flow Simulation, Needs, Achievements and Limitations. In *Proceedings of the First Pacific International Conference on Aerospace Science and Technology*, Taiwan, 1993.

[56] E. C. Marineau, G. C. Moraru, D. R. Lewis, J. D. Norris, J. D. Lafferty, and H. B. Johnson. Investigation of Mach 10 Boundary Layer Stability of Sharp Cones at Angle-of-Attack, Part 1: Experiments. In *Proceedings of AIAA SciTech 2015*, Kissimmee, Florida, 2015. AIAA-2015-1737. doi: 10.2514/6.2015-1737.

[57] J. Brooks, A. Gupta, M. S. Smith, and E. C. Marineau. Development of Non-Intrusive Velocity Measurement Capabilities at AEDC Tunnel 9. In *Proceedings of 52nd Aerospace Sciences Meeting, SciTech*, National Harbor, Maryland, 2014. AIAA-2014-1239. doi: 10.2514/6.2014-1239.

[58] J. M. Brooks, A. K. Gupta, M. S. Smith, and E. C. Marineau. Development of Particle Image Velocimetry in a Mach 2.7 Wind Tunnel at AEDC White Oak. In *Proceedings of 53nd Aerospace Sciences Meeting, SciTech*, Kissimmee, Florida, 2015. AIAA-2015-1915. doi: 10.2514/6.2015-1915.

[59] A. Walz. Compressible Turbulent Boundary Layers With Heat Transfer and Pressure Gradient in Flow Direction. *Journal of Research of the National Bureau of Standards-B*, 63B(1):53–70, 1959. doi: 10.6028/jres.063B.008.

[60] W. J. Devenport and J. A. Schetz. Boundary Layer Codes for Students in Java. In *Proceedings of the ASME Fluids Engineering Division Summer Meeting*, number FEDSM98-5139, Washington, DC, 1998. ASME.

[61] W. J. Devenport and J. A. Schetz. Heat Transfer Codes for Students in Java. In *Proceedings of the 5th ASME/JSME Thermal Engineering Joint Conference*, number AJTE99-6229, San Diego, California, 1999. ASME.

[62] R. J. Moffat. Contributions to the Theory of Single-Sample Uncertainty Analysis. *Journal of Fluids Engineering*, 104(2):250–258, 1982. doi: 10.1115/1.3241818.

[63] B. F. Bathel, P. M. Danehy, J. A. Inman, S. B. Jones, C. B. Ivey, and C. P. Goyne. Velocity Profile Measurements in Hypersonic Flows Using Sequentially Imaged Fluorescence-Based Molecular Tagging. *AIAA Journal*, 49(9):1883–1896, 2011. doi: 10.2514/1.J050722.

[64] V. Fonseca and J. Campos. Absolute Transition Probabilities of Some Kr I Lines. *Physica B+C*, 97(2):312–314, 1979. doi: 10.1016/0378-4363(79)90064-0.

[65] R. S. F. Chang, H. Horiguchi, and D. W. Setser. Radiative Lifetimes and TwoâĂŘbody Collisional Deactivation Rate Constants in Argon for Kr($4p^5 5p$) and Kr($4p^5 5pâĂš$) States. *The Journal of Chemical Physics*, 73(2):778–790, 1980. doi: 10.1063/1.440185.

[66] C. A. Whitehead, H. Pournasr, M. R. Bruce, H. Cai, J. Kohel, W. B. Layne, and J. W. Keto. Deactivation of Two-Photon Excited Xe($5p^5 6p$,6p',7p) and Kr($4p^5 5p$) in Xenon and Krypton. *The Journal of Chemical Physics*, 102(5):1965–1980, 1995. doi: 10.1063/1.468763.

[67] K. DzierżÈľga, U. Volz, G. Nave, and U. Griesmann. Accurate Transition

Rates for the 5p-5s Transitions in Kr I. *Physical Review A*, 62(2):022505, 2000. doi: 10.1103/PhysRevA.62.022505.

[68] P. G. Huang and G. N. Coleman. Van Driest Transformation and Compressible Wall-Bounded Flows. *AIAA Journal*, 32(10):2110–2113, 1994. doi: 10.2514/3.12259.

[69] P. Bradshaw. Compressible Turbulent Shear Layers. *Annual Review of Fluid Mechanics*, 9(1):33–52, 1977. doi: 10.1146/annurev.fl.09.010177.000341.

[70] H. Schlichting. *Boundary-Layer Theory*. Springer, 2000.

[71] H. H. Fernholtz and P. J. Finley. A Critical Compilation of Compressible Turbulent Boundary Layer Data. AGARD-223, 1977.

[72] H. H. Fernholtz and P. J. Finley. A Critical Commentary on Mean Flow Data for Two-Dimensional Compressible Turbulent Boundary Layers. AGARD-253, 1980.

[73] A. J. Smits and J. P. Dussauge. *Turbulent Shear Layers in Supersonic Flow*. Springer, second edition, 2006.

[74] M. V. Morkovin. Effects of compressibility on turbulent flows. *Mécanique de la Turbulence*, pages 367–380, 1962. CNRS.

[75] P. S. Klebanoff. Characteristics of turbulence in a boundary layer with zero pressure gradient. NACA TR-1247, 1955.

[76] M. Elena, J. P. Lacharme, and J. Gaviglio. Comparison of Hot-Wire and Laser Doppler Anemometry Methods in Supersonic Turbulent Boundary Layers. In *Proceedings of 2nd International Symposium on Laser Anemometry*, pages 151–157, Miami Beach, Florida, 1985.

[77] M. P. Martin. Direct Numerical Simulation of Hypersonic Turbulent Boundary Layers. Part 1. Initialization and Comparison with Experiments. *Journal of Fluid Mechanics*, 570:347–364, 2007. doi: 10.1017/S0022112006003107.

[78] J. E. Lewis, R. L. Gran, and T. Kubota. An experiment on the adiabatic compressible turbulent boundary layer in adverse and favourable pressure gradients. *Journal of Fluid Mechanics*, 51(4):657–672, 1972. doi: 10.1017/S0022112072001296.

[79] S. Xu and M. P. Martin. Assessment of Inflow Boundary Conditions for Compressible Turbulent Boundary Layers. *Physics of Fluids*, 16(7):2623–2639, 2004. doi: 10.1063/1.1758218.

[80] T. von Kármán. Turbulence and Skin Friction. *Journal of the Aeronautical Sciences*, 1(1):1–20, 1934. doi: 10.2514/8.5.

[81] K. E. Schoenherr. *Resistance of Flat Surfaces Moving Through a Fluid*, volume 40. 1932.